

Creep–Fatigue Interaction of Inconel 718 Manufactured by Electron Beam Melting

Stefan Guth,* Tomáš Babinský, Steffen Antusch, Alexander Klein, Daniel Kuntz, and Ivo Šulák

Electron beam melting of Ni-base superalloy Inconel 718 allows producing a columnar-grained microstructure with a pronounced texture, which offers exceptional resistance against high-temperature loading with severe creep–fatigue interaction arising in components of aircraft jet engines. This study considers the deformation, damage, and lifetime behavior of electron-beam-melted Inconel 718 under in-phase thermomechanical fatigue loading with varying amounts of creep–fatigue interaction. Strain-controlled thermomechanical fatigue tests with equal-ramp cycles, slow–fast cycles, and dwell time cycles are conducted in the temperature range from 300 to 650 °C. Results show that both dwell time and slow–fast cycles promote intergranular cracking, gradual tensile stress relaxation, as well as precipitate dissolution and coarsening giving rise to cyclic softening. The interplay of these mechanisms leads to increased lifetimes in both dwell time and slow–fast tests compared to equal ramp tests at higher strain amplitudes. Conversely, at lower mechanical strain amplitudes, the opposite is observed. A comparison with results of conventional Inconel 718 indicates that the electron-beam-melted material exhibits superior resistance against strain-controlled loading at elevated temperatures such as thermomechanical fatigue.

unprecedented design freedom with reduced material waste during production,^[1] but also because they enable to tailor material microstructures fit for specific in-service needs.^[2–4]

Inconel 718 is the most frequently applied Ni-base superalloy for jet engine components and is commonly used for turbine discs. Its microstructure is strengthened by coherent precipitates of γ'' -phase (Ni_3Nb) and to a lesser extent of γ' -phase ($\text{Ni}_3(\text{Al},\text{Ti})$), which provides excellent strength at elevated temperatures. During high-temperature exposure, the metastable γ'' precipitates may transform into stable but incoherent δ precipitates with identical Ni_3Nb composition, thus reducing the strengthening effect.^[5] Therefore, the strength of Inconel 718 drops rapidly at higher temperatures^[6] and its application temperature is limited to about 650 °C. Due to its favorable weldability, Inconel 718 is well suited for AM and it has been largely investigated in various AMed forms in the past decade.^[7] A remarkable feature

1. Introduction

To enhance the sustainability of aircraft jet engines and comparable hot-going systems, recent developments aim to prolong the service life of critical components while simultaneously minimize material usage. Additive manufacturing (AM) technologies offer great potential to reach these goals. Not only due to their

of Inconel 718 processed by powder bed fusion processes, for example, selective laser melting (SLM) or electron beam melting (EBM), is a texture with a preferential $\langle 001 \rangle$ -orientation along the building direction, which arises from the directional heat flow during production.^[2,8,9] Particularly, EBM allows producing a microstructure with columnar grains that resembles that of directionally solidified (DS) alloys.^[10] Similar to DS alloys, such a columnar microstructure with a $\langle 001 \rangle$ texture maybe beneficial under fatigue and creep loading.^[2,11] From a $\langle 001 \rangle$ -texture follows a low elastic modulus in loading direction, which reduces stress and plastic strain under strain-controlled fatigue loading,^[12] while there are only few grain boundaries perpendicular to the loading direction, which are prone to creep damage.

Although there are numerous investigations on the mechanical behavior of additively manufactured Inconel 718,^[7] only few studies consider the behavior under near-service conditions of hot-going components. In service, these experience temperature gradients during start-up, load change, and shutdown operations, which create thermal strain gradients inducing thermal stresses. Repeating these operations leads to a thermomechanical fatigue (TMF) loading of the material, where strain and temperature cycles arise simultaneously and which often determine the service lifetime. When strain and temperature are in phase, that is, high

S. Guth, S. Antusch, A. Klein, D. Kuntz
Institute for Applied Materials
Karlsruhe Institute of Technology
Engelbert-Arnold-Straße 4, 76131 Karlsruhe, Germany
E-mail: stefan.guth@kit.edu

T. Babinský, I. Šulák
Institute of Physics of Materials
Czech Academy of Sciences
Žitkova 22, 616 00 Brno, Czech Republic

 The ORCID identification number(s) for the author(s) of this article can be found under <https://doi.org/10.1002/adem.202300294>.

© 2023 The Authors. Advanced Engineering Materials published by Wiley-VCH GmbH. This is an open access article under the terms of the Creative Commons Attribution License, which permits use, distribution and reproduction in any medium, provided the original work is properly cited.

DOI: 10.1002/adem.202300294

temperatures coincide with tensile stress and strain, substantial creep–fatigue interaction may arise and reduce the lifetime. Due to the high complexity of TMF laboratory tests, less complex isothermal low-cycle-fatigue (LCF) tests are often employed to simulate TMF loading. High-temperature LCF studies on Inconel 718 have shown that for a given strain range, the lifetimes of EBM-manufactured specimens with columnar microstructure loaded along the preferential grain orientation exceed those of conventional wrought specimens as well as those of EBM specimens loaded transverse to the preferential grain orientation.^[10,13] Similarly, crack propagation tests under dwell-fatigue conditions have shown that EBM specimens outperform conventional ones as well as specimens manufactured by SLM.^[14] This emphasizes the potential of the columnar-grained Inconel 718 manufactured by EBM. For conventional Inconel 718, Deng et al.^[15] found that particularly in-phase TMF is more damaging than isothermal low-cycle fatigue at the maximum temperature of the TMF cycle. At constant temperature, intergranular damage occurring in tension may be counterbalanced in compression,^[16] while under in-phase TMF loading, the temperature in the compressive part of the cycle is too low for that.^[17] Consequently, when substantial creep–fatigue interaction occurs, design based on isothermal data may be nonconservative. When tensile dwell times (DTs) are introduced in LCF or TMF cycles, creep–fatigue interaction increases and the resulting lifetimes are typically reduced.^[18–21] A study by Ngala and Maier^[16] on isothermal creep–fatigue interaction on the ODS Ni-base superalloy P1000 showed that so-called slow–fast cycles where the loading rate in the tensile-going part of the cycle is lower than in the compression-going part resulted in even lower lifetimes than cycles with equal ramps (ERs) and additional tensile dwells. Similar results were found in isothermal fatigue tests on Ni-base superalloy MAR-M247 at 750 °C.^[22] The assumed reason for this behavior is that a cycle with a slow tensile-going part produces higher intergranular crack propagation rates than a fast tensile-going part followed by tensile dwell. The results of Ngala and Maier^[15] also showed that the lifetimes for in-phase TMF tests were in between those for isothermal slow–fast tests and those for isothermal tests with ERs. To our knowledge, results on the influence of slow–fast cycles under TMF conditions on the lifetime of high-temperature alloys have not been published so far.

In this study, we investigate the creep–fatigue interactions of columnar-grained Inconel 718 manufactured by EBM under near-service loading conditions. TMF tests under in-phase conditions with optional DTs at maximum temperature and with optional slow tensile-going cycle parts were conducted. The resulting TMF lifetimes are discussed with respect to the evolution of microstructure and damage. The goal is to understand how creep and fatigue mechanisms interact for the unique microstructure of EBM-manufactured Inconel 718. Eventually, the insights may be applied to optimize the EBM manufacturing of the material for applications with severe creep–fatigue interaction.

2. Experimental Section

2.1. Specimen Manufacturing

The raw specimens were manufactured in near-net-shape geometry by an EBM facility of type Arcam A2X from GE Additive

(formerly Arcam AB). The building direction was parallel to the loading axis of the specimens. The powder of type Arcam Inco 718 was supplied by Arcam EBM, Sweden, and exhibited granular sizes between 45 and 106 μm. **Table 1** shows the chemical composition of the powder given by the supplier. All element contents were within the limits specified in ASTM F3055.^[23] During building, layers of 70 μm thickness were laid on the building plate made of stainless steel. In the beginning, the building plate was heated to 1000 °C. The manufacturing of the Inconel 718 parts was performed with default process parameters of the system, which included a beam speed of 4530 mm s^{−1}, a beam current of 15 mA, a focus offset of 7.5 mA, and a speed function of 94. At the frame of each specimen built, three layers with a contour scanning strategy were applied according to the standard settings of the EBM facility.

After building, the raw specimens were hot isostatically pressed (HIP) for 4 h at 1120 °C and 100 MPa in order to reduce porosity. Subsequently, a standard heat treatment for Inconel 718 (given by GE Additive) was applied, which comprised a solution annealing of 2 h at 1065 °C followed by two-stage aging of 8 h at 718 °C and 8 h at 621 °C and eventually cooling in air. From the raw specimens, fatigue-testing specimens with a gauge length of 10 mm and a gauge length diameter of 4.3 mm were machined. The amount of material removal was chosen so that the contour region was completely removed and a cleanly machined surface in the gauge length without any remaining defects of EBM manufacturing was achieved. Hence, the surface quality of the raw specimens had no influence on the test results. The goal of the study was to test the EBM microstructure and not the surface quality.

2.2. Thermomechanical Fatigue Testing

The TMF tests were conducted under strain control on a servo-electric 100 kN Zwick testing machine in laboratory air. A capacitive extensometer with 10 mm gauge length was attached to the gauge length using alumina rods to measure and control the total strain. The specimens were heated with a high-frequency induction system, while cooling was achieved by thermal conduction into the water-cooled grips. The temperature was measured and controlled with a ribbon-type Ni–CrNi (Type K) thermocouple that was wrapped around the center of the gauge length. Both hydraulic grips and specimen shoulders were profiled in order to guarantee stable fixation during testing. **Figure 1** shows a picture of a mounted specimen in the TMF testing machine.

The temperature range for all tests was 300–650 °C. The maximum temperature of 650 °C represents a demanding application temperature for Inconel 718, while the minimum temperature of 300 °C was to represent a short shut down of a turbine engine. The phase angle between mechanical strain and temperature for all tests was 0°, that is, the loading was in-phase and maximum strain

Table 1. Chemical composition of the Inconel 718 powder applied for EBM process in wt%.

C	Cr	Mo	Nb + Ta	Ti	Al	Ni	O	Fe
0.04	18.70	2.99	5.02	0.96	0.55	52.61	0.012	Bal.

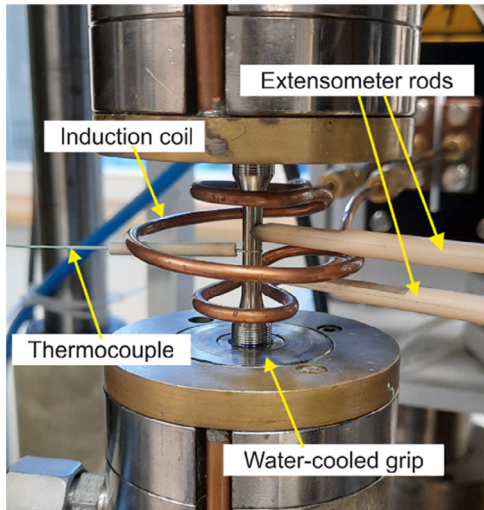


Figure 1. TMF test setup before test start.

coincided with maximum temperature. **Figure 2** shows a schematic representation of the tested cycle types. Three cycle forms with varying expected amounts of creep-fatigue interaction were tested. 1) Triangular ER cycles with a temperature rate of 5 K s^{-1} . 2) DT cycles with trapezoidal waveform including ramps with 5 K s^{-1} and a DT at maximum temperature of 600 s. 3) Slow-fast (SF) cycles featuring a sawtooth shape including a slow heating rate of 0.52 K s^{-1} and a fast cooling rate of 5 K s^{-1} . The resulting cycle time was 140 s for ER cycles and 740 s for DT and SF cycles, respectively. It was expected that the portion of creep damage increased in the order $\text{ER} < \text{SF} < \text{DT}$. For all test types, the mechanical load was symmetrical ($R_\epsilon = -1$) and started at the mean temperature of $475 \text{ }^\circ\text{C}$.

Prior to each test, the thermal strain ϵ_{th} during a cycle was determined by applying the temperature cycle under controlled zero force. The controlling total strain was then calculated by adding the desired mechanical strain ($\epsilon_{\text{t}} = \epsilon_{\text{th}} + \epsilon_{\text{me}}$). Before the actual load

cycles, five load-free cycles were conducted to establish thermal equilibrium of the test setup. The tested mechanical strain amplitudes $\epsilon_{\text{a,me}}$ varied between 0.4 and 0.8%, resulting in cycles to failure between about 200 and 10 000. The mechanical strain ϵ_{me} comprised an elastic part ϵ_{e} and a plastic part ϵ_{p} . The plastic strain amplitude $\epsilon_{\text{a,p}}$ was determined as half width of the stress-strain hysteresis loop at the mean stress level. The number of cycles to failure N_f , which will be used synonymously with lifetime, was determined by the following procedure. The maximum stress occurring in each cycle was plotted over the cycle number in a linear diagram. Through the part of the plot, which was identified as stabilized, a straight regression line was fit and set down by 10%. The cycle in which the measured maximum stress falls for the first time below the value given by the set-down regression line was defined as N_f .

2.3. Analysis

Representative fatigue specimens were longitudinally and transversally cut and subsequently analyzed by means of electron microscopy. The initial state and later the imposed fatigue and creep-fatigue damage were characterized using scanning electron microscopy LYRA 3 XMU FEG/SEMxFIB (SEM) equipped with electron backscatter diffraction (EBSD) detector Symmetry by Oxford Instruments, which was utilized for texture analyses. The microstructure and its evolution was captured on thin foils using transmission electron microscopes (TEM) JEOL JEM-2100F and Thermo Scientific Talos F200i operating at 200 kV. Both TEMs are equipped with bright-field and dark-field detectors allowing observation in scanning mode (STEM).

3. Results

3.1. Initial State

Figure 3 summarizes the initial state of the fatigue specimens after manufacturing.

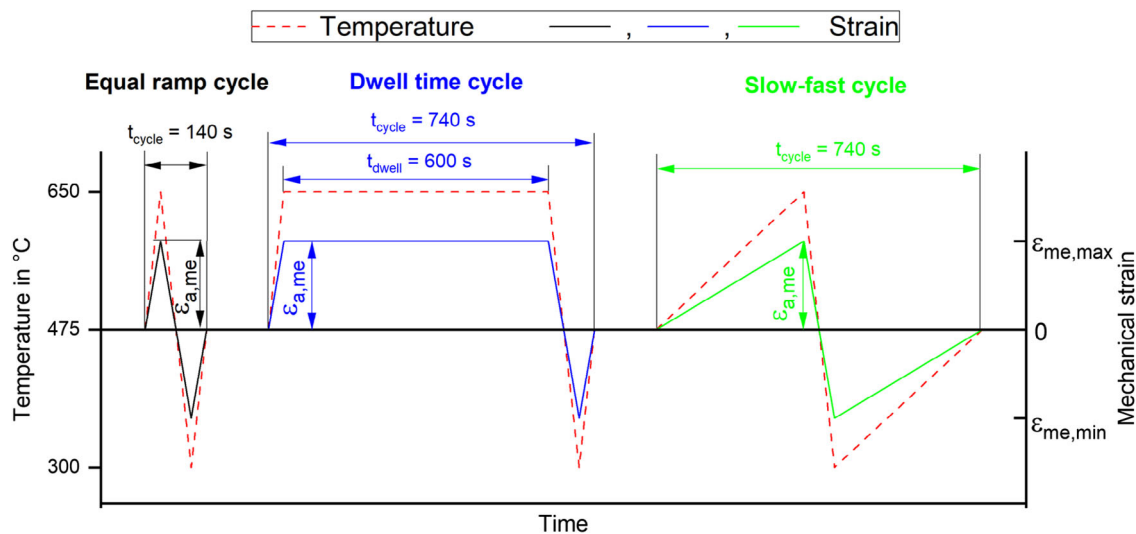


Figure 2. Time courses of temperature and strain for the investigated cycle types. The phase angle between temperature and strain was always $0^\circ = \text{in-phase loading}$.

Figure 3a shows the raw electron beam melted specimens on the building plate. In Figure 3b, a cross section of a heat-treated gauge length can be seen, revealing some defects near the raw surface but very low porosity in the core area. Figure 3c,d show EBSD inverse pole figure (IPF) maps of a longitudinal and a cross section, respectively. While the grains appear equiaxed in view parallel to the building direction, most of them are significantly elongate in the building direction. This is reflected by the average grain size, which was measured using EBSD images to be about $40\ \mu\text{m}$ perpendicular to the building direction and $120\ \mu\text{m}$ parallel to the building direction. The grain sizes parallel to the building direction range from about $10\ \mu\text{m}$ up to more than $1.5\ \text{mm}$, while the grain size distribution perpendicular to the building direction is more homogeneous. Comparing the microstructure of specimens in as-printed state and after the HIP and heat treatment showed that the average grain size increased by about 5% perpendicular to the building direction and by about 30% parallel to the building direction due to the HIP and heat treatment. A comparison with the IPF legend reveals a strong texture in

a $\langle 001 \rangle$ -direction, which corresponds to the building direction. There are some areas where the grains are less elongate in the building direction and exhibit no distinct texture. EBSD measurements before and after HIP and heat treatment revealed that the treatments had no significant influence on the texture. It is noteworthy that no annealing twins could be observed in any specimen. Figure 3e,f show TEM bright-field pictures of the microstructure. Figure 3e indicates that there are cell structures within grains with coarser δ precipitates forming the cell walls and finely dispersed γ' and γ'' precipitates in the cell volume. The detail presented in Figure 3f shows that the γ' precipitates have a cuboidal form, while γ'' and δ precipitates appear ellipsoidal or disc shaped, the latter being coarser. Since creep-fatigue damage is expected to occur predominantly in intergranular areas, the initial state of the grain boundaries is of particular interest. In general, the grain boundaries are smooth without marked serrations. Energy-dispersive X-ray spectroscopy analyses (not shown here) confirmed that there are no significant differences of the chemical composition between matrix and grain

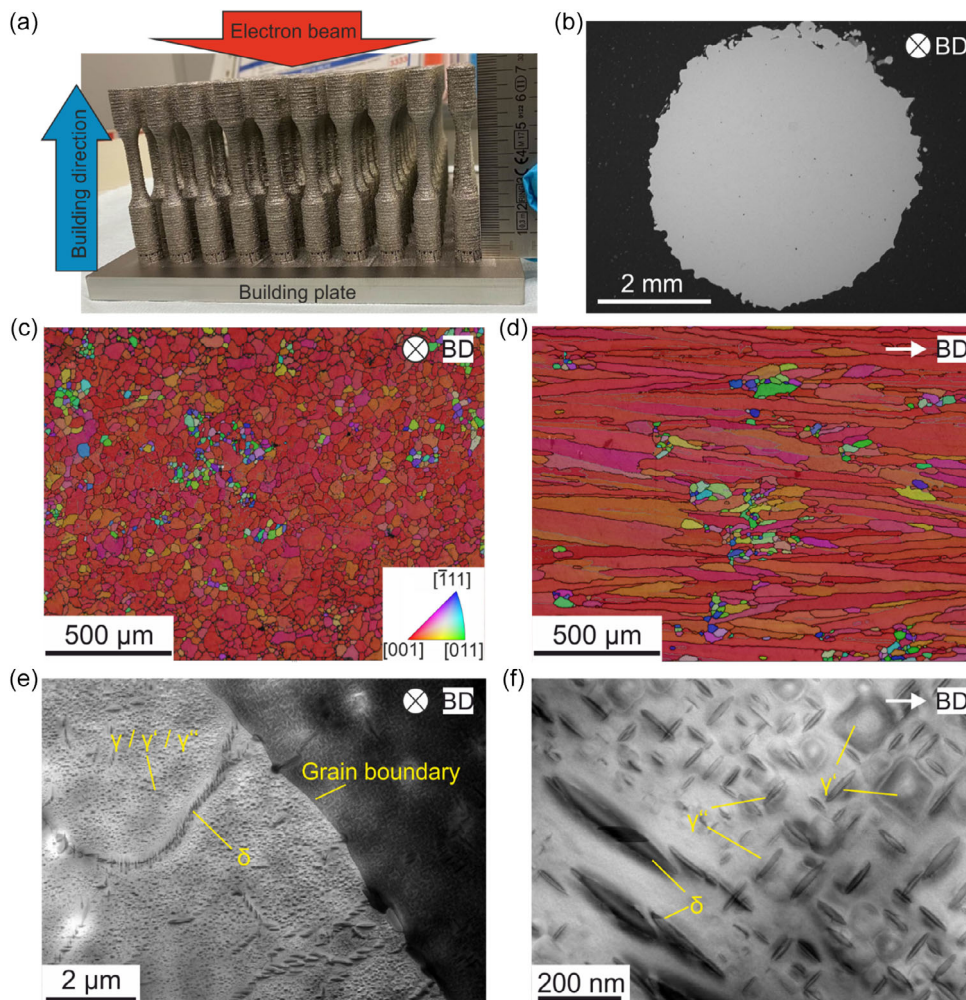


Figure 3. Initial state of Inconel 718 EBM before testing. a) Specimens after EBM manufacturing. b) SEM view of cross section of a specimen gauge length after HIP and heat treatment. c,d) EBSD IPF maps of cross (c) and longitudinal (d) section after HIP and heat treatment. The IPF legend in (c) is also valid for (d). e) TEM bright-field micrograph of microstructure after HIP and heat treatment. f) Detailed TEM bright-field micrograph showing precipitate structure and distribution after HIP and heat treatment.

boundaries. Figure 3e shows that there are carbides on the grain boundaries; however, in contrast to the cell walls, there is no preferential δ -phase precipitation. Occasionally, Laves-phase precipitates with sharp and edgy needle shape could be found on grain boundaries.

Density measurements of the machined specimens using the Archimedes method yielded a value of $8190 \pm 15 \text{ kg m}^{-3}$. Considering the density of conventional Inconel 718 of 8220 kg m^{-3} ,^[6] this suggests a high relative density above 99.5%, which could be expected due to the HIP treatment. The elastic modulus of the individual EBM specimens was evaluated prior to testing from the unloading curve of a 3 kN load, resulting in a stress of about 200 MPa, which is safely in the elastic region. The measured room-temperature mean value of the elastic modulus was $144.9 \pm 3.6 \text{ GPa}$, which is significantly lower than the elastic modulus of conventionally manufactured Inconel 718, for which a value of 200 GPa is typical.^[6]

3.2. Thermomechanical Fatigue Lifetime

Figure 4 shows the obtained TMF lifetimes dependent on the mechanical strain amplitude for the different cycle types. Unexpectedly, for mechanical strain amplitudes of 0.6 and

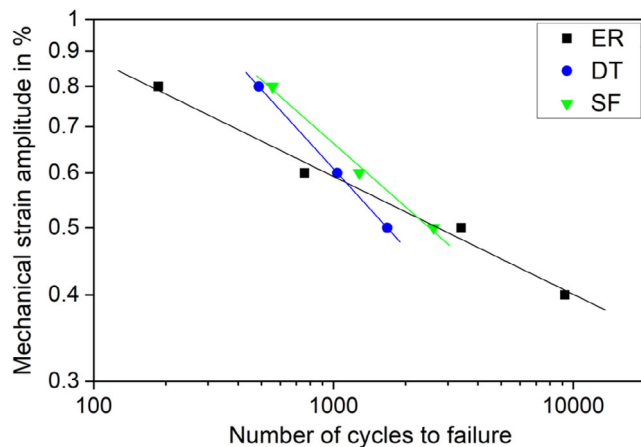


Figure 4. Influence of cycle type and mechanical strain amplitude on the TMF lifetime under in-phase conditions.

0.8%, both introducing DTs and slow tensile loading increase the lifetimes. For lower mechanical strain amplitudes, the positive effect on lifetime due to DTs and slow tensile loading becomes less and eventually at $\epsilon_{a,me} = 0.5\%$, the lifetimes for DT and SF cycling are shorter than for ER cycling. Hence, the slope of the life curves for SF and DT cycling is higher than for ER cycling resulting in crossovers between $\epsilon_{a,me} = 0.5$ and 0.6% , respectively. For all strain amplitudes tested, DT lifetimes were shorter than SF lifetimes. SF and DT tests at $\epsilon_{a,me} = 0.4\%$ were not conducted due to the expected extremely long test duration of more than 6 weeks.

3.3. Cyclic Deformation Behavior

Figure 5 shows representative stress–strain hysteresis loops for the different cycle types in the first cycle and at half of the lifetime, respectively. Generally, the deformation is even at the relatively high applied mechanical strain amplitude of 0.6%, mainly elastic, and the loops are only slightly opened. This reflects the high strength of the material in combination with the relatively low elastic modulus along the loading direction. For ER cycling, the stress–strain course does not change markedly from the first to the half lifetime cycle, indicating a stable cyclic behavior. For DT cycling, the plastic strain amplitude is higher than for the other cycle types because of the stress relaxation and the corresponding accumulation of plastic strain during the dwells. At half of the lifetime, the DT hysteresis loop shifted by more than 100 MPa toward the compressive regime and the plastic strain amplitude increased from 0.036 to about 0.06%. Under SF loading, the loop in the first cycle looks very similar to the one under ER loading. However, at half of the lifetime, the loop slightly shifted to the compressive regime.

The developments of stress amplitude and mean stress shown in Figure 6 confirm the findings from the hysteresis loops. For ER cycling at $\epsilon_{a,me} = 0.6\%$ both stress amplitude and mean stress are stable until the macroscopic crack initiation. For SF cycling, the mean stress decreases slightly with increasing cycle number, while for DT cycling it decreases significantly. Already the initial mean stress is in all cases negative, which is typical for in-phase TMF loading since both the elastic modulus and the material strength decrease with increasing temperature; hence, the induced stress at maximum (tensile) strain is lower than at

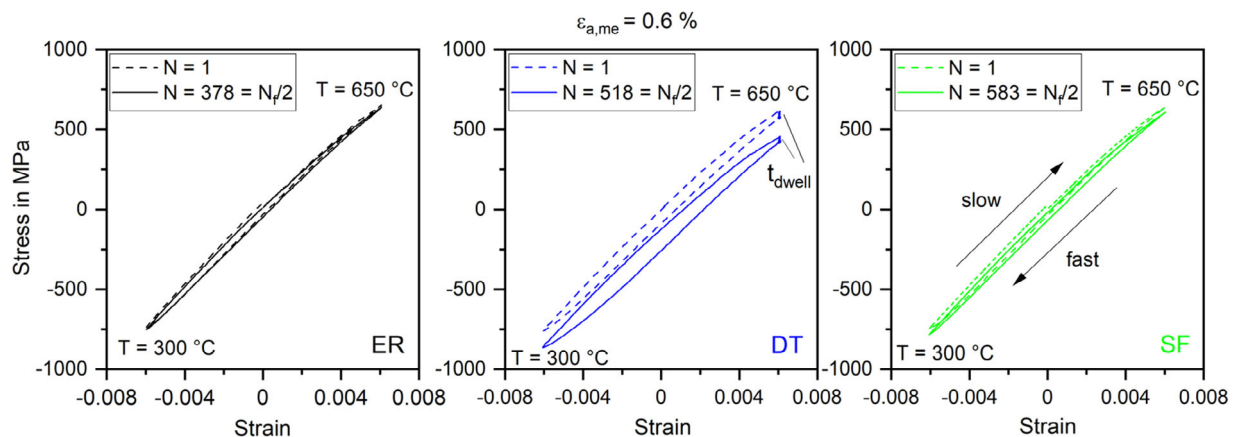


Figure 5. Influence of the cycle type on the development of stress–strain hysteresis loops at a mechanical strain amplitude of 0.6%.

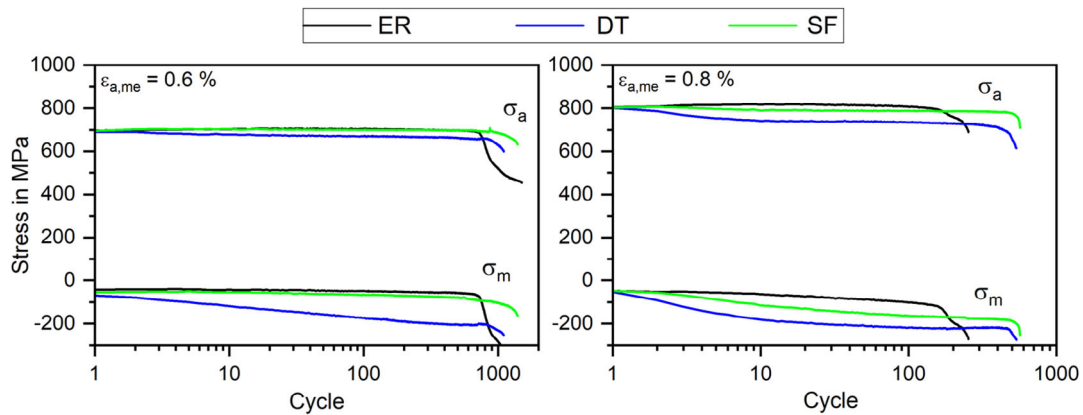


Figure 6. Influence of the cycle type on the cyclic deformation curves for a mechanical strain amplitude of 0.6% (left) and 0.8% (right).

minimum (compressive) strain. For $\epsilon_{a,me} = 0.8\%$, there is a slight cyclic hardening and slight compressive mean stress development under ER loading. Under DT loading, both cyclic softening and compressive mean stress development are more pronounced than for $\epsilon_{a,me} = 0.6\%$. For SF loading with $\epsilon_{a,me} = 0.8\%$ there is also a more pronounced compressive mean stress development than for $\epsilon_{a,me} = 0.6\%$ and a slight cyclic softening. For all cycle types, the initial values of stress amplitude and mean stress are very similar and the differences develop during cycling.

3.4. Microstructural Evolution

Figure 7 shows representative STEM bright-field images from longitudinal foils after TMF testing with different cycle types.

ER cycling with the high mechanical strain amplitudes of 0.8 and 0.6% produced a high amount of dislocations, which are occasionally arranged in persistent slip bands (PSBs) parallel to (111) planes of the matrix, as shown in Figure 7a. The detailed image shown in Figure 7b reveals a generally high dislocation density after ER cycling with high mechanical strain amplitudes. The morphology of the γ' and γ'' precipitates is mostly similar to the initial condition (Figure 3f). However, both γ' and γ'' precipitates are frequently sheared by dislocations and some of the γ' precipitates have coarsened. After ER cycling with lower strain amplitudes as well as after DT and SF cycling, no PSBs were observed and the dislocation density was generally lower. Comparing the microstructure after ER cycling with the low mechanical strain amplitude of 0.4% (Figure 7c) with the initial state, Figure 3f indicates that the amount of cuboidal γ'

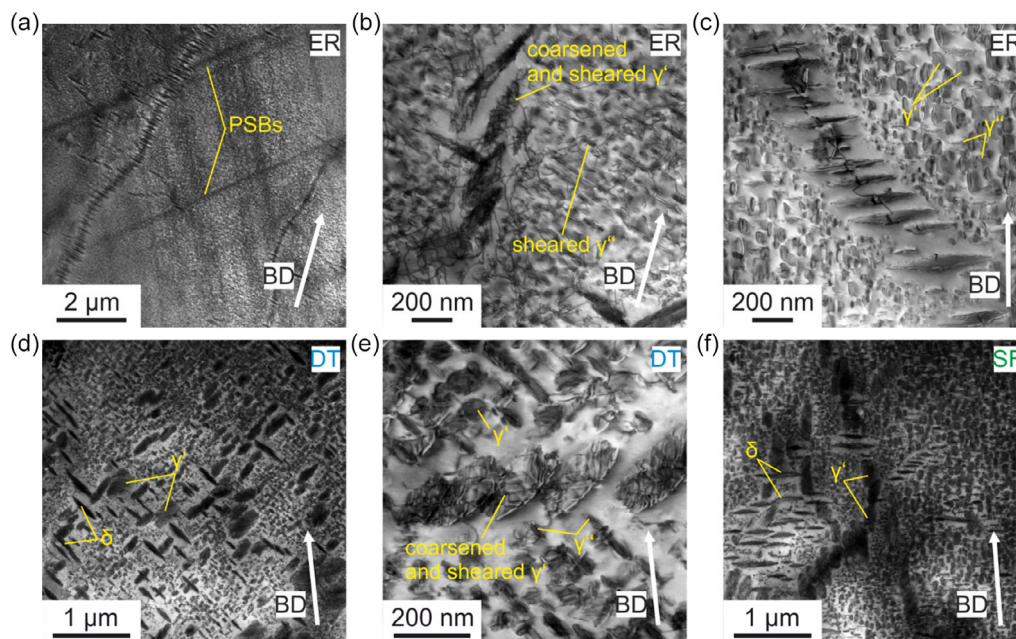


Figure 7. STEM micrographs showing microstructural evolution due to in-phase TMF cycling with different loading cycles. a,b) ER cycling with $\epsilon_{a,me} = 0.8\%$, $N_f = 186$; c) ER cycling with $\epsilon_{a,me} = 0.4\%$, $N_f = 9225$; d,e) DT cycling with $\epsilon_{a,me} = 0.8\%$, $N_f = 488$; f) SF cycling with $\epsilon_{a,me} = 0.8\%$, $N_f = 557$. The loading axis is parallel to the building direction.

precipitates increased at the expense of the amount of disc-shaped γ'' precipitates. The microstructure after both DT and SF cycling appears similar with a reduced amount of γ'' phase and numerous coarser γ' precipitates, see Figure 7d,f. The detail in Figure 7e shows that dislocations often shear these coarser γ' precipitates. In all cases, the δ precipitates appear to be relatively stable when compared to their initial state. Since they are incoherent to the matrix, they are not sheared by dislocations.

3.5. Damage Observation

Figure 8 shows representative damage forms observed with SEM after TMF loading. For ER cycling, cracks propagate in mixed transgranular and intergranular mode. Figure 8a illustrates this behavior with transgranular crack initiation starting from a surface extrusion and subsequent intergranular propagation after the crack intersected a grain boundary. Surface extrusions

approximately inclined by 45° to the loading axis could be frequently observed after ER cycling with $\epsilon_{a,me} = 0.6$ and 0.8% . In many cases, cracks started from these extrusions. For all other loading conditions, no extrusions could be found. The fracture surface of an ER specimen shown in Figure 8b features striations, which are typical for transgranular cracking as well as facets indicating intergranular fracture. Figure 8c shows internal creep damage in the form of cavities on carbide–matrix interfaces as well as on grain boundaries after ER loading. DT and SF cycling produced significantly more internal damage than ER cycling. Figure 8d shows internal cavity damage along with cracks that propagate apparently along grain boundaries. The EBSD IPF map in Figure 8e shows that the internal damage occurs mainly at grain boundaries, that is, the damage is intergranular. Further, the intergranular damage concentrates in areas where the grains are less elongate in the building direction and do locally not exhibit the $\langle 001 \rangle$ -texture. Figure 8f shows an

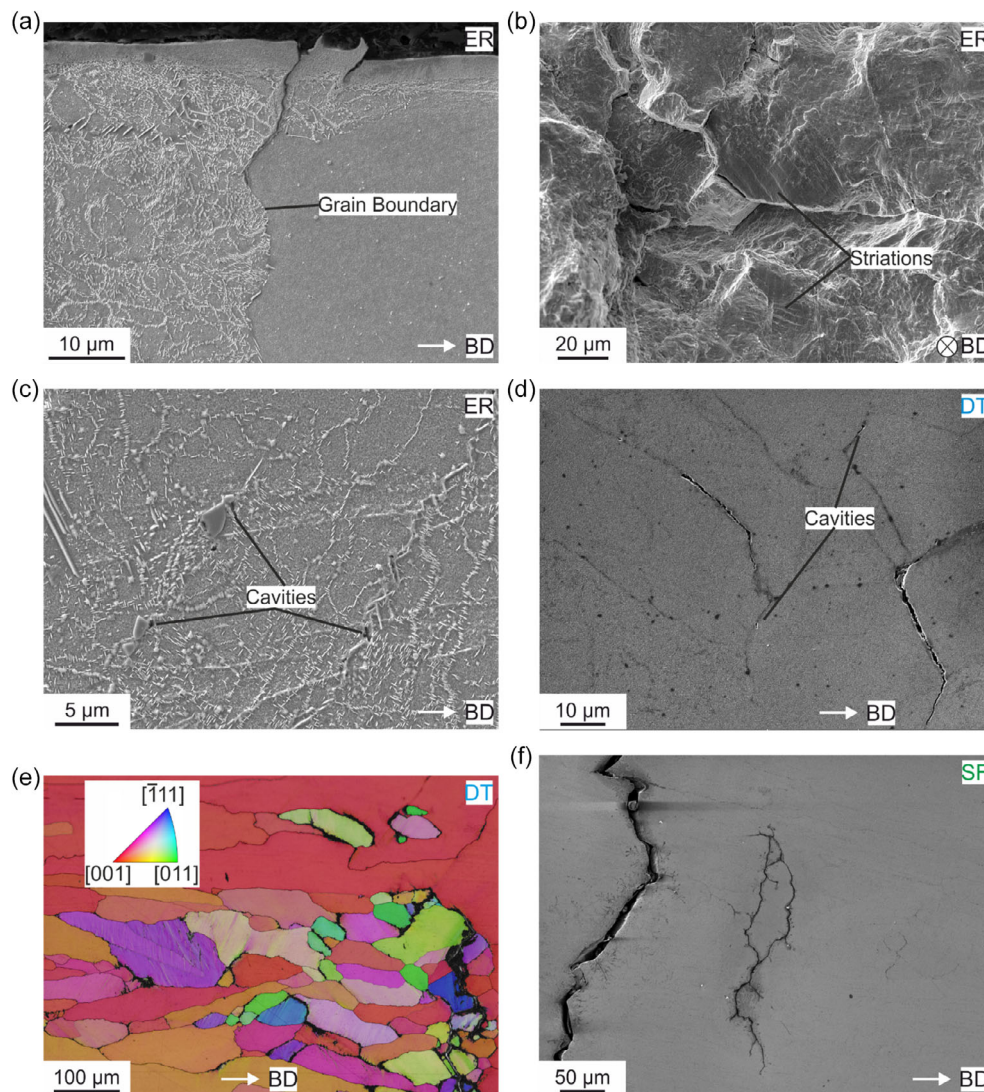


Figure 8. Damage evolution during TMF-IP cycling with different loading cycles. a) Longitudinal section and b) fracture surface after ER cycling with $\epsilon_{a,me} = 0.8\%$, $N_f = 186$; c) longitudinal section ER cycling with $\epsilon_{a,me} = 0.4\%$, $N_f = 9225$; d) longitudinal section and e) EBSD IPF map after DT cycling with $\epsilon_{a,me} = 0.8\%$, $N_f = 488$; f) longitudinal section after SF cycling with $\epsilon_{a,me} = 0.8\%$, $N_f = 557$.

intergranular crack network, which has formed after SF loading. In general, the damage appearance after DT and SF cycling was similar. Damage emerging from the occasional Laves-phase precipitates on the grain boundaries was not observed.

4. Discussion

4.1. Microstructural Evolution and Cyclic Deformation

The initial state of the testing material featuring a pronounced $\langle 001 \rangle$ texture as well as the columnar-grained structure along the building direction is typical for EBM-manufactured Inconel 718.^[9,24,25] The texture and the low elastic modulus in [001]-direction for Ni-base alloys^[26] are responsible for the relatively low elastic modulus along the loading axis of the specimens when compared to conventional Inconel 718 without texture. Hence, for a given mechanical strain amplitude, the EBM material yields lower stress amplitudes and plastic strain amplitudes (Figure 5 and 6) than conventional Inconel 718 under similar loading conditions.^[15]

The microstructural observations show that the cycle type significantly affects the evolution of the microstructure, which is reflected in the deformation behavior. SF cycles and particularly DT cycles feature longer periods at elevated temperatures favoring diffusion processes. In combination with severe plastic deformation and the corresponding dislocation movements, this leads to shearing and coarsening of γ' precipitates, while γ'' precipitates may dissolve after shearing and fragmenting (Figure 7). Coarsening of γ' precipitates is a typical aging effect of Inconel 718,^[27] which may be promoted by severe plastic deformation. Shearing and dissolution of γ'' precipitates have been reported for isothermal fatigue tests on conventional Inconel 718 at temperature around 650 °C.^[19,28] Further, long periods at elevated temperatures allow dislocations to rearrange and possibly annihilate, which is reflected in the generally lower dislocation densities after SF and DT cycling. To a lesser extent, γ' coarsening and γ'' dissolution occurs also for long-running ER tests, when the accumulated time at elevated temperatures is sufficient (see Figure 7c). Coarsening and shearing of γ' -precipitates, dissolution of γ'' precipitates, as well as reduced dislocation densities are the mechanisms, leading to the observed cyclic softening in SF and DT tests with high mechanical strain amplitudes (Figure 6). For lower mechanical strain amplitudes, coarsening of precipitates presumably also leads to material softening in SF and DT tests; however, this is not reflected in the evolution of the stress amplitude since the deformation is mainly elastic, that is, the flow stress is not reached. Xiao et al. similarly reported a tendency to reduced cyclic softening with decreasing mechanical strain amplitude in isothermal fatigue tests of conventional Inconel 718 at 647 °C.^[28] The formation of PSBs observed in ER tests with high mechanical strain amplitudes is typical for cyclically deformed Inconel 718 in conventional^[29] as well as in additively manufactured form.^[8,30] The presumable reason for the slight cyclic hardening observed in the ER test with $\epsilon_{a,me} = 0.8\%$ is the increase of dislocation density due to severe plastic deformation. It has to be noted that competing softening mechanisms, that is, precipitate shearing, dissolution, and coarsening, are also effective under ER loading (see

Figure 7a,b). During ER tests with mechanical strain amplitudes below 0.6%, PSBs were not observed, presumably because the accumulated plastic strain and thus the overall dislocation movement is not sufficient. During SF and DT testing, longer times at elevated temperatures facilitate cross slip and climb mechanisms. Therefore, dislocation movement is more homogenous and PSBs do not form. In isothermal tests on Ni-base alloy MAR-M247, similarly much less PSBs after SF and DT testing than after ER testing were reported.^[22]

A further effect of the longer periods at elevated temperatures in SF and DT tests is that the tensile stress acting at elevated temperatures relaxes due to creep deformation. The plastic tensile strain accumulated during this process is not fully reversed during the compressive part of the cycle where the temperatures are lower so that the material is stronger and creep deformation is restricted. Furthermore, the fast cycling without dwells in the compressive regime for both SF and DT tests offers less time for compressive creep deformation. Therefore, in SF and particularly in DT test, the hysteresis loops shift gradually to the compressive region (center diagram of Figure 5). The process continues up to the point when either the tensile stress has become too low to drive further creep deformation or the compressive stress reaches the flow stress so that the creep strain is reversed by low-temperature plasticity.^[17] Consequently, at a given mechanical strain amplitude, the saturated maximum stress dependent on the cycle type increases in the order $DT < SF < ER$.

Tensile stress relaxation and a gradually increasing compressive mean stress due to creep deformation are typical for in-phase TMF testing of high-strength superalloys.^[17] The effects can be also observed in isothermal high-temperature tests, when tensile dwells are introduced, while compressive loading and unloading are continuous, that is, an asymmetrical cycle shape favoring tensile creep deformation is applied.^[22]

4.2. Damage Evolution and Lifetime

The damage observations show that both introducing DTs and slow tensile loading increase the amount of intergranular cracking due to creep damage on grain boundaries (Figure 8). Formation and coalescence of grain boundary pores facilitating grain boundary cracking are a typical effect of both high-temperature dwells and slow tensile loading.^[16,31] For conventional Inconel 718, a higher share of intergranular cracking due to DTs was found to increase crack propagation rates under in-phase TMF loading.^[32] Therefore, shorter lifetimes in SF and DT tests than in ER tests were expected. However, for high mechanical strain amplitudes, the contrary was observed. Reasons for this are the lower maximum stresses and stress amplitudes due to tensile stress relaxation and cyclic softening in SF and DT tests when compared to ER tests (see Section 4.1.). In TMF tests on wrought Ni-base alloy NiCr22Co12Mo9, increased lifetimes due to introducing tensile dwells were similarly associated with cyclic softening effects due to the dwells.^[33] Another reason for shorter ER lifetimes at high mechanical strain amplitudes is early crack initiation from PSBs forming extrusions at the surface (Figure 8a). This mechanism was observed exclusively for ER tests with $\epsilon_{a,me} = 0.6$ and

0.8% and may outweigh the negative effects of increased intergranular crack propagation in SF and DT tests. Results of isothermal fatigue test at 550 °C on EBM Alloy 718 showing significantly reduced lifetimes when cracks started from slip bands at the surface rather than from internal inclusions support this assumption.^[13] A further root cause for the unexpected lifetime increase in SF and DT tests may be the columnar grain structure of the investigated material. In creep tests on EBM Inconel 718 at 650 °C, Shassere et al. found significantly longer rupture times for material with elongate grains than for material with equiaxed grains.^[11] Saarimäki et al. reported significantly higher crack propagation rates for fine-grained than for coarse-grained conventional Inconel 718 under isothermal fatigue loading at 550 °C.^[34] Deng et al. compared the crack propagation rates of EBM Inconel 718 under dwell-fatigue conditions at 550 °C for specimen orientations with grain elongation parallel and perpendicular to the loading direction. They found that that cracks propagate at lower rate when the grains are elongated parallel to the loading direction, that is, when cracks face only few grain boundaries perpendicular to the loading direction. Moreover, they reported that both EBM directions outperform conventional Inconel 718, owing to the much higher grain size of the EBM specimens.^[35] This suggests that the reduced amount of grain boundaries perpendicular to the loading direction of the present material may impede creep-fatigue-induced grain boundary damage, thus attenuating lifetime-reducing effects of DTs and slow tensile loadings. The assumption is supported by the fact that intergranular damage after SF and DT testing concentrates in areas where the grains are less elongate and do not exhibit a <001>-texture (Figure 8e). Accordingly, an optimized building procedure minimizing the amount of equiaxed grains without texture should allow for a material with even further increased creep-fatigue resistance. A further reason for the excellent creep-fatigue resistance of EBM Inconel 718 may be the fact that the grain boundaries contain only small amounts of the δ -phase, which may offer a preferential crack path.^[36] At lower mechanical strain amplitudes, PSBs were not observed and both cyclic softening and tensile stress relaxation are less pronounced since the deformation is mainly elastic. Moreover, longer lifetimes associated with lower mechanical strain amplitudes allow for increased time-dependent damage mechanisms such as creep pore formation on grain boundaries, preferential grain boundary, and crack tip oxidation. The combination of these effects leads to the observed crossover of SF/DT and ER lifetime curves (Figure 4). Since in SF tests most of the slow tensile loading occurs at temperatures where detrimental creep-fatigue interactions are negligible, SF lifetimes are longer than DT lifetimes. Under isothermal fatigue loading the opposite may occur.^[16,22]

One notable aspect of the investigated material is its absence of twins even after the HIP and heat treatment. This may be beneficial for its fatigue resistance since potentially crack-inducing slip bands have been found to initiate at annealing twins in conventional Ni-base alloys.^[37,38] Gribbin et al. attributed short low-cycle-fatigue lifetimes of direct metal laser-sintered and HIPed Inconel 718 to crack initiation on annealing twins, which formed during the HIP treatment.^[39] In order to reveal the influence of twins on the fatigue properties, a direct comparison between a material with and without twins is necessary. In other studies on AM Inconel 718, twins formed after HIP at

Table 2. Relationship between lifetime, mechanical strain amplitude, and half-life stress amplitude for EBM and conventionally forged Inconel 718.^[15]

Material	Mechanical strain amplitude in %	Half-life stress amplitude in MPa	Cycles to failure
EBM Inconel 718	0.4	499.5	9225
	0.6	697	757
	0.8	808	186
Conventional Inconel 718 ^[15]	0.4	627.5	1550
	0.6	805	200
	0.8	903.5	85

temperatures above 1150 °C,^[8,39] while the material in the present study was HIPed at 1120 °C. Therefore, the key to form twins in EBM Inconel 718 may be increased temperature during HIP.

Table 2 compares the present results of EBM Inconel 718 under ER loading with those of conventionally forged Inconel 718 under TMF in-phase loading with identical maximum temperature and heating/cooling rate.^[15] Considering the strain-life relationship, the EBM material performs markedly better, particularly at lower mechanical strain amplitudes. In terms of stress-life behavior, both materials are comparable. This indicates that the better strain-life behavior of the EBM material can be largely attributed to its low elastic modulus in loading direction resulting in lower-induced stresses. As discussed earlier, the elongate grain structure of the EBM material may be an advantage over conventional material with equiaxed grains under loading conditions with severe creep-fatigue interaction. To clarify this, further work with a direct comparison of EBM and conventional Inconel 718 under SF and DT loading conditions is necessary. Based on the results at hand, EBM Inconel 718 performs comparable or even superior to conventional Inconel 718 when subjected to creep-thermomechanical fatigue loading.

5. Conclusion

Strain-controlled in-phase thermomechanical fatigue tests in a temperature range of 300–650 °C with equal-ramp, dwell time, and slow-fast cycles were conducted on electron-beam-melted Ni-base alloy Inconel 718 in order to study creep-fatigue interactions. The results highlight the potential of EBM Inconel 718 as a promising alternative to conventionally manufactured Inconel 718. The following main conclusions can be drawn. 1) Typical for EBM manufacturing, the specimens exhibit elongate grains with only few grain boundaries perpendicular to the loading direction and a pronounced <001> texture resulting in a low elastic modulus in loading direction. The synergistic effects of these characteristics render the material exceptionally resistant against strain-controlled loading with severe creep-fatigue interaction such as in-phase thermomechanical fatigue. 2) Under equal-ramp loading, cracks propagate in mixed transgranular and intergranular mode. Introducing DTs or slow tensile loading ramps promotes intergranular cracking due to creep cavity formation and coalescence on grain boundaries. The intergranular damage concentrates in areas of less elongate grains. A manufacturing

process minimizing such areas may further enhance the creep fatigue resistance of the material. 3) Longer periods at elevated temperature in DT and slow-fast tests promote tensile stress relaxation and cyclic softening due to coarsening and dissolution of the strengthening γ' and γ'' precipitates. At high mechanical strain amplitudes, these mechanisms reduce the acting maximum stress and stress amplitude, which counterbalances the additional intergranular damage and leads to unexpectedly longer lifetimes in DT and slow-fast tests when compared to equal-ramp tests. 4) At lower mechanical strain amplitudes, introducing DTs or slow tensile loading ramps reduces the lifetime since the deformation is mainly elastic; thus, tensile stress relaxation and cyclic softening are less pronounced. On the other hand, time-dependent creep and oxidation damage mechanisms are more relevant due to the generally longer testing times.

Acknowledgements

This work was financially supported by the European Union H2020 Twinning project SIRAMM (H2020-WIDESPREAD-2018-03 no. 857124). Open Access funding enabled and organized by Projekt DEAL.

Conflict of Interest

The authors declare no conflict of interest.

Data Availability Statement

The data that support the findings of this study are available from the corresponding author upon reasonable request.

Keywords

additive manufacturing, creep-fatigue interaction, damage mechanisms, Inconel 718, thermomechanical fatigue

Received: March 1, 2023

Revised: April 13, 2023

Published online:

- [1] T. D. Ngo, A. Kashani, G. Imbalzano, K. T. Q. Nguyen, D. Hui, *Composites, Part B* **2018**, *143*, 172.
- [2] V. A. Popovich, E. V. Borisov, A. A. Popovich, V. S. Sufiarov, D. V. Masaylo, L. Alzina, *Mater. Des.* **2017**, *114*, 441.
- [3] Z. Li, Y. Cui, W. Yan, D. Zhang, Y. Fang, Y. Chen, Q. Yu, G. Wang, H. Ouyang, C. Fan, Q. Guo, D.-B. Xiong, S. Jin, G. Sha, N. Ghoniem, Z. Zhang, Y. M. Wang, *Mater. Today* **2021**, *50*, 79.
- [4] J. Berry, A. Perron, J.-L. Fattebert, J. D. Roehling, B. Vrancken, T. T. Roehling, D. L. Rosas, J. A. Turner, S. A. Khairallah, J. T. McKeown, M. J. Matthews, *Mater. Today* **2021**, *51*, 65.
- [5] M. Sundararaman, P. Mukhopadhyay, S. Banerjee, *Metall. Trans. A* **1988**, *19*, 453.
- [6] Special Metals, *INCONEL Alloy 718*, Publication Number SMC-045, Huntington, USA **2007**.
- [7] E. Hosseini, V. A. Popovich, *Addit. Manuf.* **2019**, *30*, 100877.
- [8] M. E. Aydinöz, F. Brenne, M. Schaper, C. Schaak, W. Tillmann, J. Nellesen, T. Niendorf, *Mater. Sci. Eng. A* **2016**, *669*, 246.
- [9] D. Deng, J. Moverare, R. L. Peng, H. Söderberg, *Mater. Sci. Eng., A* **2017**, *693*, 151.
- [10] M. M. Kirka, D. A. Greeley, C. Hawkins, R. R. Dehoff, *Int. J. Fatigue* **2017**, *105*, 235.
- [11] B. Shassere, D. Greeley, A. Okello, M. Kirka, P. Nandwana, R. Dehoff, *Metall. Mater. Trans. A* **2018**, *49*, 5107.
- [12] F. E. H. Müller, M. Heilmaier, L. Schultz, *Mater. Sci. Eng., A* **1997**, *234–236*, 509.
- [13] H. Kjellson, A. R. Balachandramurthi, J. Moverare, T. Hansson, *Metall. Mater. Trans. A* **2022**, *53A*, 2496.
- [14] D. Deng, R. L. Peng, J. Moverare, *Mater. Sci. Eng. A* **2020**, *797*, 140072.
- [15] W. Deng, J. Xu, Y. Hu, Z. Huang, L. Jiang, *Mater. Sci. Eng. A* **2019**, *742*, 813.
- [16] W. O. Ngala, H. J. Maier, *Mater. Sci. Eng. A* **2009**, *510–511*, 429.
- [17] S. Guth, S. Doll, K.-H. Lang, *Mater. Sci. Eng., A* **2015**, *642*, 42.
- [18] S. Guth, R. Petráš, V. Škorík, T. Kruml, J. Man, K.-H. Lang, J. Polák, *Int. J. Fatigue* **2015**, *80*, 426.
- [19] K. Barat, S. Sivaprasad, S. K. Kar, S. Tarafder, *Fatigue Fract. Eng. Mater. Struct.* **2019**, *42*, 2823.
- [20] E. Sadeghi, G. Asala, P. Karimi, D. Deng, J. Moverare, T. Hansson, *Mater. Sci. Eng., A* **2021**, *827*, 142051.
- [21] I. Šulák, K. Obrtlík, *Int. J. Fatigue* **2023**, *166*, 107238.
- [22] I. Šulák, K. Obrtlík, T. Babinský, S. Guth, *Int. J. Fatigue* **2022**, *164*, 107133.
- [23] ASTM F3055, *Standard Specification for Additive Manufacturing Nickel Alloy (UNS N07718) with Powder Bed Fusion*, ASTM International, West Conshohocken, USA **2021**.
- [24] L. A. Al-Juboori, T. Niendorf, F. Brenne, *Metall. Mater. Trans. B* **2018**, *49B*, 2969.
- [25] S.-H. Sun, Y. Koizumi, T. Saito, K. Yamanaka, Y.-P. Li, Y. Cui, A. Chiba, *Addit. Manuf.* **2018**, *23*, 457.
- [26] C. Kumara, D. Deng, J. Moverare, P. Nylén, *Mater. Sci. Technol.* **2018**, *34*, 529.
- [27] K. Kulawik, P. A. Buffat, A. Kruk, A. M. Wusatowska-Sarnek, A. Czyrska-Filemonowicz, *Mater. Charact.* **2015**, *100*, 74.
- [28] L. Xiao, D. L. Chen, M. C. Chaturvedi, *Mater. Sci. Eng., A* **2008**, *483–484*, 369.
- [29] L. Xiao, D. L. Chen, M. C. Chaturvedi, *Scr. Mater.* **2005**, *52*, 603.
- [30] M. S. Dodaran, M. Muhammad, N. Shamsaei, S. Shao, *Int. J. Fatigue* **2022**, *162*, 107002.
- [31] I. Šulák, K. Obrtlík, *Eng. Fract. Mech.* **2017**, *185*, 92.
- [32] J. J. Moverare, D. Gustafsson, *Mater. Sci. Eng., A* **2011**, *528*, 8660.
- [33] S. Guth, K.-H. Lang, *Mater. Sci. Eng., A* **2020**, *794*, 139970.
- [34] J. Saarimäki, M. Lundberg, J. J. Moverare, *Adv. Eng. Mater.* **2018**, *20*, 1700930.
- [35] D. Deng, R. L. Peng, J. Moverare, *Mater. Sci. Eng., A* **2019**, *760*, 448.
- [36] J. Saarimäki, J. Moverare, R. Eriksson, S. Johansson, *Mater. Sci. Eng., A* **2014**, *612*, 398.
- [37] J. C. Stinville, E. Martin, M. Karadge, S. Ismonov, M. Soare, T. Hanlon, S. Sundaram, M. P. Echlin, P. G. Callahan, W. C. Lenthe, V. M. Miller, J. Miao, A. E. Wessman, R. Finlay, A. Loghin, J. Marte, T. M. Pollock, *Acta Mater.* **2018**, *152*, 16.
- [38] M. A. Charpagne, J. M. Hestroffer, A. T. Polonsky, M. P. Echlin, D. Texier, V. Valle, I. J. Beyerlein, T. M. Pollock, J. C. Stinville, *Acta Mater.* **2021**, *215*, 117037.
- [39] S. Gribbin, J. Bicknell, L. Jorgensen, I. Tsukrov, M. Knezevic, *Int. J. Fatigue* **2016**, *93*, 156.